Stabilizing an Ultracold Fermi Gas against Fermi Acceleration to Superdiffusion through Localization

S. Barbosa[,1] M. Kiefer-Emmanouilidis[,1,2,3] F. Lang[,1] J. Koch[,1] and A. Widera[1,*]

[1]*Department of Physics and Research Center OPTIMAS, RPTU Kaiserslautern-Landau, 67663 Kaiserslautern, Germany*
[2]*Department of Computer Science and Research Initiative QC-AI, RPTU Kaiserslautern-Landau, 67663 Kaiserslautern, Germany*
[3]*Embedded Intelligence, German Research Centre for Artificial Intelligence, 67663 Kaiserslautern, Germany*

Anderson localization, i.e., destructive quantum interference of multiple-scattering paths, halts transport entirely. Contrarily, time-dependent random forces expedite transport via Fermi acceleration, proposed as a mechanism for high-energy cosmic rays. Their competition creates interesting dynamics, but experimental observations are scarce. Here, we experimentally study the expansion of an ultracold Fermi gas inside time-dependent disorder and observe distinct regimes from sub- to superdiffusion. Unexpectedly, quantum interference counteracts acceleration in strong disorder before a transition to a diffusive state occurs in the driven system. Our system enables the investigation of Fermi acceleration in the quantum-transport regime.

Brownian diffusion, its microscopic understanding, and its application to macroscopic problems enabled the emergence and development of modern science [1,2]. Commonly, the diffusive motion of a particle inside a medium is characterized in d dimensions by its position variance $\sigma^2(t) - \sigma^2(0) = 2dDt$, increasing linearly with time t and diffusion coefficient D. Although successful in describing diffusion across many fields, fascinating phenomena deviating from this behavior have been found and studied extensively in a plethora of systems [3,4], including cosmic rays [5], animals' foraging behavior [6,7], stock-market fluctuations [8], turbulent-plasma transport [9], and molecular motion in cells [10]. Typically, a single regime of this so-called anomalous diffusion emerges. This Letter demonstrates how we employ a cosmological effect to control the properties and type of anomalous diffusion in an ultracold quantum gas, providing a first step to better understand and investigate dynamical phase transitions, fundamental transport behaviors, and even simulate the aforementioned systems. Anomalous diffusion can be characterized by the value of the diffusion exponent α in a generalized power law [3,4],

$$\sigma^2(t) - \sigma^2(0) = 2dD_\alpha t^\alpha, \qquad (1)$$

where D_α is a generalized diffusion coefficient and the system lies in the regime of subdiffusion (superdiffusion) for $\alpha < 1$ ($\alpha > 1$).

Perhaps the most extreme form of subdiffusion is the perfect absence of diffusion ($\alpha = 0$) for quantum particles undergoing Anderson localization (AL) inside disorder [11,12]. Here, multiple scattering of a particle's wave function from the disordered environment leads to destructive interference everywhere except for the particle's initial position, resulting in the complete halt of transport. Interference-induced localization has been observed in classical waves such as ultrasound [13,14], microwaves [15], and light [16–19] as well as in quantum matter using ultracold atoms [20–23]. Further, in three dimensions, a transition from the diffusive to the localized regime occurs at a threshold energy called mobility edge [12]. Particles are expected to undergo subdiffusion near that transition point until they become fully localized [24]. Although decades of theoretical and experimental research have passed [12], previous observations of AL [25] and especially whether particles in the interacting case may localize [26–28] are widely questioned.

Going beyond static disorder, the impact of spatiotemporal noise on AL and the transition to delocalization has been investigated intensively [29,30]. In the past decade, the destruction of AL by temporal variation of an underlying disorder potential was studied, particularly in optical systems [31]. Remarkably, random time-varying environments or fluctuating force fields have been found to drive particle acceleration in outer space, explaining high-energy cosmic rays [32–35]. This fundamental mechanism, which has come to be known as Fermi acceleration, dates back to Fermi [32] and was later studied in detail for classical and quantum particles scattered in time-varying potentials [36–39]. Microscopically, a particle scattered from a copropagating potential maximum decelerates, while it accelerates for collisions from counterpropagating potential
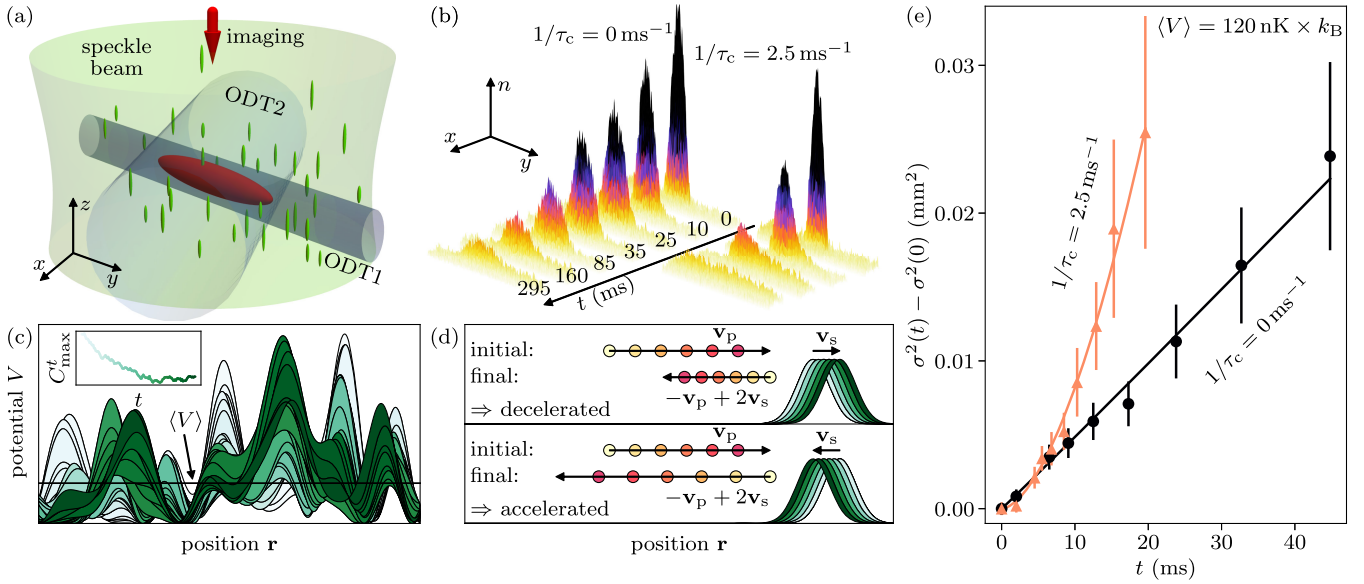
FIG. 1. (a) Sketch of atom cloud (red ellipsoid), optical dipole traps (ODT1, ODT2), speckle laser beam (green), and anisotropic speckle grains (small green ellipsoids). Imaging is performed along the $-z$ direction (red arrow). (b) Recorded density distribution for different expansion duration t for $1/\tau_c = 0$ ms^{-1} (left) and $1/\tau_c = 2.5$ ms^{-1} (right). The length along the y axis is 1 mm. For each setting of t and $1/\tau_c$, 50 repetitions are averaged. For increased image clarity, the illustration was smoothed by a Gaussian filter with a standard deviation of one pixel only for this figure. The asymmetric profiles after expansion occur due to the inhomogeneous speckle-beam envelope causing an asymmetric acceleration for large $1/\tau_c$. This effect does not affect the analysis significantly. (c) Visualization of the disorder's time evolution from a 1D numerical simulation. Lines are snapshots along the evolution; later times correspond to darker green. Both peak heights and positions vary with different rates. The black horizontal line marks the time-constant average disorder potential $\langle V \rangle$. Inset shows $C_{\max}^t$ in arbitrary units over t (same color scale) [48,49]. (d) Illustration of Fermi acceleration: rear-end collisions (top) effectively decelerate, while head-on collisions accelerate the particle. Colors indicate time as before. (e) Measured cloud variance over time from the data sets shown in (b). Power-law fits (lines) to the data (points) yield diffusion exponents $\alpha = 1.02 \pm 0.04$ for $1/\tau_c = 0$ ms^{-1} (circles) and $\alpha = 1.70 \pm 0.08$ for $1/\tau_c = 2.5$ ms^{-1}. Error bars indicate 1σ statistical uncertainty.

maxima. Statistically, the counterpropagating collisions are more probable with increasing particle velocity. On average, particles moving in time-varying potentials experience a net accelerating force. This mechanism has since been generalized to the classical Fermi-Ulam-accelerator model [40,41], which was later expanded to include quantum dynamics [42,43]. Moreover, diffusion inside such a time-varying random disorder is expected to exhibit universal behavior with $\sigma^2 \sim t^2$ and $\langle v^2 \rangle \sim t^{2/5}$ [36–38,44] if $d > 1$, where $\langle v^2 \rangle$ is the variance of velocity.

Previous theoretical works have considered the diffusion of quantum gases through speckles [45] or in periodically modulated disorder [46]. However, the expansion in continuously evolving disorder has only been studied for classical particles [39], and experimental investigations are scarce in general. Here, we investigate the expansion of an ultracold noninteracting Fermi gas in a time-varying disorder potential, studying the competition of localization effects with the acceleration due to stochastic Fermi acceleration by tracing the diffusion of the gas.

Experimentally, we produce a degenerate Fermi gas of ^{6}Li atoms at a temperature $T \approx 0.1 T_F < 100$ nK, with Fermi temperature $T_F = E_F/k_B$, Fermi energy E_F and Boltzmann constant k_B. All $N \approx 10^5$ atoms are prepared spin-polarized in the lowest-lying Zeeman substate. Our sample is well approximated by an ideal Fermi gas due to its fermionic nature, as s-wave interactions are prohibited entirely due to the Pauli exclusion principle and p-wave and higher-order interactions are strongly suppressed at these low temperatures [24]. Initially, the atoms are prepared in a crossed-dipole trap; see Fig. 1(a). By extinguishing one trap beam at time $t = 0$, the trap instantly becomes shallow along the y axis while the remaining directions remain effectively unchanged. Hence, the atoms start to expand along the y direction; see Figs. 1(b) and 1(e). After a variable expansion duration, we probe the cloud's extension through absorption imaging along the z axis [47].

Additionally at $t = 0$, we quench on a repulsive optical speckle disorder potential $V(\mathbf{r})$, created by 532 nm laser light; see Refs. [48,49] for details. Spatially, it consists of anisotropic grains with typical sizes of $\eta_{x,y}^2 \times \eta_z = (750$ nm$)^2 \times 10.2$ µm, where $\eta_{x,y}$ and η_z are the correlation lengths along the respective directions [50,51]. We characterize the strength of the disorder by its spatial average $\langle V \rangle$. Furthermore, our speckle disorder can continuously decorrelate into other, new realizations over time by employing two diffusor plates that rotate relative to each other [48,49]; see Fig. 1(c). While the disorder potential's

statistical properties (such as $\eta_{x,y,z}$ and $\langle V \rangle$) remain constant, the local details change significantly with time. We characterize the rate at which this change occurs via the decorrelation rate $1/\tau_c$, defined as the inverse time after which the cross-correlation peak height C_{max}^t has decayed to half its initial value at $t = 0$; see inset of Fig. 1(c) and Refs. [48,49] for technical details. Hence, we realize a time-varying stochastic force field for our atom cloud, allowing for stochastic Fermi acceleration [Fig. 1(d)]. We achieve decorrelation rates up to $1/\tau_c = 3.5 \text{ ms}^{-1}$ to study the effect on the diffusion of noninteracting atoms in either weak ($\langle V \rangle = 120 \text{ nK} \times k_B \approx 0.2 E_F$) or stronger ($\langle V \rangle = 400 \text{ nK} \times k_B \approx 0.5 E_F$) disorder [52]. We note that, even in the static case, our three-dimensional blue-detuned disorder potential does not allow for classically bound states. Since classical trapping occurs only for much larger disorder strengths, it can be neglected for all cases considered here [53,54]. Importantly, the atom cloud never crosses into the regimes of dimensionality lower than $d = 3$. Still, we analyze the diffusive expansion only along one dimension, $d = 1$, as the atoms cannot expand along the x and z directions. From the absorption images taken, we extract the cloud width σ. While standard methods such as the fitted Gaussian width or the participation ratio work in principle, we use the so-called inverse participation width (see Refs. [52,55] for details), which is particularly suited to compensate for image noise, becoming relevant for long expansion times, when the local cloud density decreases.

In Fig. 2, the dynamics of cloud variances σ^2 are shown for (a) weak and (b) strong disorder. The data from the expansion in static disorder, $1/\tau_c = 0 \text{ ms}^{-1}$, is shown as black points. It exhibits the lowest exponent for both disorder strengths, allowing for the longest observation times. The observation time is technically limited by atom losses or the finite size of the camera detection area and the envelope of the disorder speckle pattern [55]. Nevertheless, we observe various transient transport regimes. When we increase the decorrelation rate toward its maximum value of $1/\tau_c = 3.5 \text{ ms}^{-1}$, we recover a strongly increased slope and, therefore, exponent for both disorder strengths. In fact, the slope even takes on the same value as in the disorder-free expansion, i.e., ballistic transport. This conforms with the predicted transport universality of $\sigma^2 \sim t^2$ for time-dependent force fields [36–38,44].

To compare the experimental data to expectations derived from Fermi acceleration, we perform a Markov-chain Monte Carlo simulation employing the minimal stochastic model of Ref. [44]. We simulate classical point particles scattering with randomly moving large spheres; see Appendix A. The simulation yields the same accelerating behavior as seen in the experimental data; see Fig. 2(c). This comparison, reinforces that Fermi acceleration is indeed the underlying acceleration mechanism.

A quantitative analysis of the change of dynamical regimes seen in Fig. 2 is done by extracting the diffusion
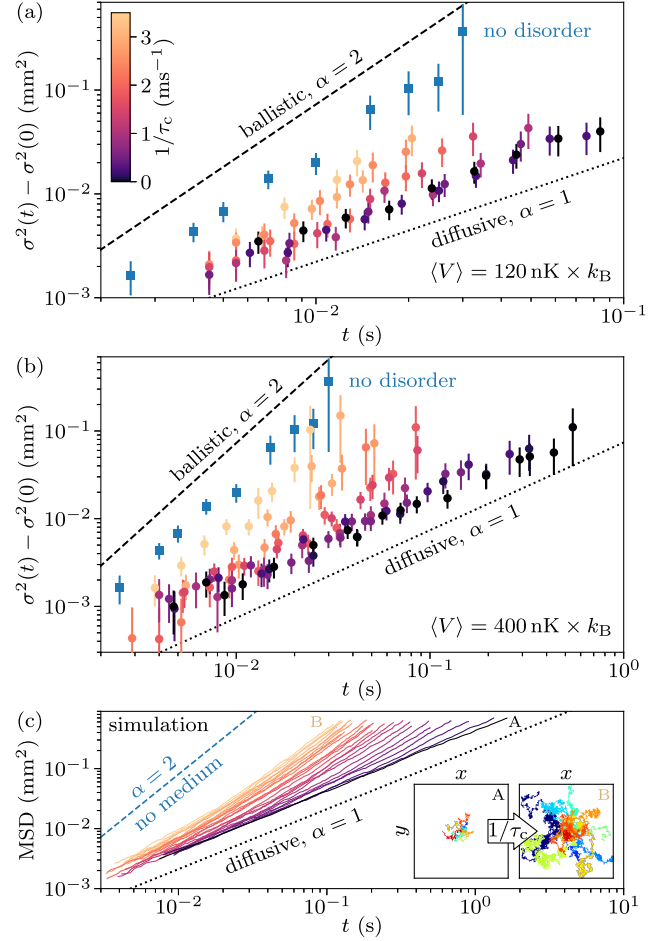

FIG. 2. Experimental cloud variances (points) for different decorrelation rates [color bar in (a)] for (a) $\langle V \rangle = 120 \text{ nK} \times k_B$, and (b) $\langle V \rangle = 400 \text{ nK} \times k_B$. Blue squares show variances from disorder-free expansion [55]. Error bars indicate 1σ statistical uncertainty. The slope of the black dotted (dashed) line indicates the exponent α of Eq. (1) for normal (ballistic) diffusion. Specifically, the black data points show a slight but significant subdiffusion [see also Fig. 3(c)], which is observed for a broad parameter range compatible to localization in static disorder as shown in Ref. [55]. (c) Particle-averaged mean squared displacement (MSD) from a single simulation run for 25 velocity scales of the medium, ranging from the static case (A) to the experimentally maximum-achievable dynamics (B) (color scale as for the experimental data). The dashed blue line shows free expansion without a medium. Inset: 12 examples of simulated trajectories up to $t = 100$ ms for the static (A, left) and maximally dynamic case (B, right) from which we calculate MSD. Both boxes are of size $1 \text{ mm} \times 1 \text{ mm}$.

exponent α and coefficient D_α from the different series of each $\langle V \rangle$ and $1/\tau_c$. The exponent α is obtained as the slope from linear regression of the logarithm of both variance and time. With that, we calculate the anomalous diffusion coefficient as $D_\alpha = \langle (\sigma^2(t) - \sigma^2(0))/2t^\alpha \rangle$, where the set of values that are averaged is constant in time. Note that D_α has the unit $\text{m}^2 \text{ s}^{-\alpha}$ [3].
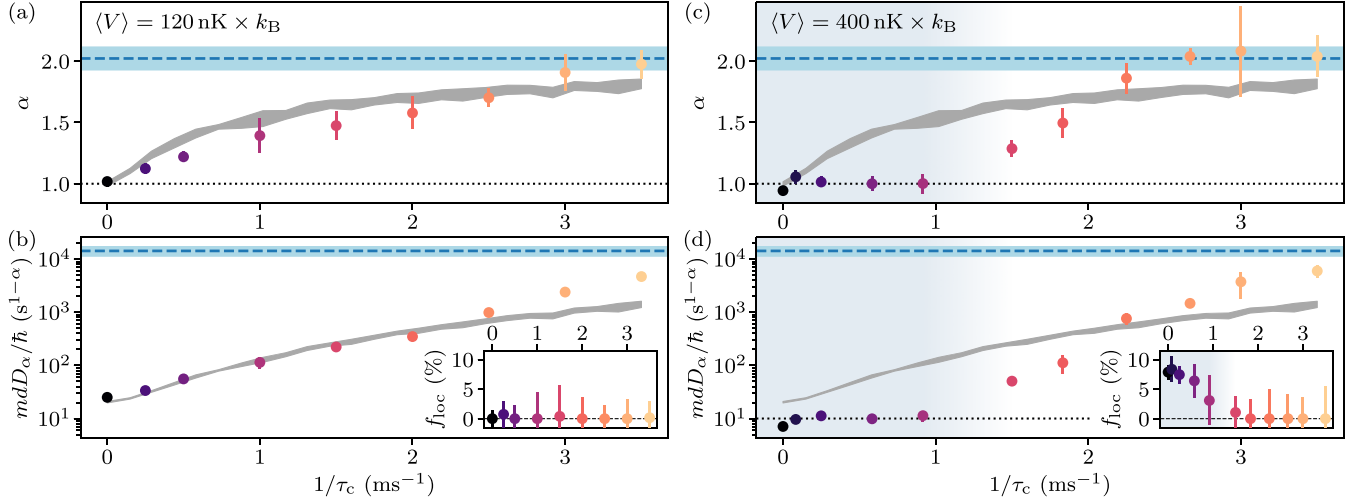
FIG. 3. Diffusion properties in (a),(b) weak disorder, $\langle V \rangle = 120$ nK $\times k_B$, and (c),(d) strong disorder, $\langle V \rangle = 400$ nK $\times k_B$. (a),(c) Diffusion exponents α as a function of decorrelation rate $1/\tau_c$ from measurements (dots) and simulation of 12 trajectories (gray area). The blue dashed line indicates the disorder-free measurement, and the blue area around is its error as shown in Ref. [55]. Error bars and areas represent 1σ statistical uncertainty. (b),(d) Normalized diffusion coefficient $mdD_\alpha/\hbar$ with the same colors and line types as in panel (a). For the experimental data (simulation), $d = 1$ ($d = 2$); see End Matter for details. Experimental errors are calculated as the standard deviation of values used for averaging. Insets show the localized fraction f_{loc} (Appendix B). For weak disorder, in (b), $f_{loc} \approx 0$ for all decorrelation rates. For strong disorder, in (d), we observe a significant $f_{loc} > 0$, which vanishes at $1/\tau_c \approx 1$ ms^{-1}, coinciding with the transition from a constant to a significant increase in both the diffusion exponent and coefficient. The shading highlights this quantum-transport region in (c),(d).

For the expansion in weak disorder, we see a direct and monotonous increase of both α and D_α with $1/\tau_c$; see Figs. 3(a) and 3(b). This directly reflects a kinetic-energy gain increasing with the decorrelation rate. We can tune the exponent through the entire range of superdiffusion with values between $\alpha = 1$ for static, weak disorder and $\alpha = 2$ by choice of $1/\tau_c$. The simulation predicts this tunability well, even agreeing quantitatively with the experimental data for a wide range of $1/\tau_c$.

We find a strikingly different behavior in strong disorder. For static disorder, $1/\tau_c = 0$ ms^{-1}, we find the system to be slightly but statistically significantly in the subdiffusive regime with $\alpha = 0.94 \pm 0.03$; see Fig. 3(c). As reported by Ref. [24], subdiffusion is expected to occur near the mobility edge until the wave packet has expanded into its fully localized state. We refer to Ref. [55], where we performed a thorough study of the expansion in static disorder of various strengths. A widely used estimate for AL is the Ioffe-Regel criterion, comparing the disorder transport length l to a particle's wave number k. Localization is expected to occur for $kl \sim 1$ and below. This criterion can be expressed for ^{6}Li as $T < 160$ nK for the geometric mean of the correlation lengths $\bar\eta$ of our speckle disorder ($T < 900$ nK for η_y, along the expansion axis) [23]. Since the gas temperature is $T < 100$ nK, our system fulfills the Ioffe-Regel criterion. An alternative criterion regards the critical momentum k_{AL} below which AL is expected to occur [45]. Specifically for our case $\langle V \rangle / E_c > 1$, with correlation energy $E_c = \hbar^2/(m\eta^2)$, we

can estimate $k_{AL} \approx (\langle V \rangle / E_c)^{2/5}/\eta$, where $\hbar$ is the reduced Planck constant and m is the atomic mass. The largest momentum in our gas is the Fermi momentum k_F, and we find $k_F \approx 2k_{AL}$ for $\bar\eta$ (and $k_F \approx 0.8k_{AL}$ for η_y). Hence, we can expect a significant fraction of the low-energy fermions to localize [55]. Therefore, we attribute the onset of subdiffusion for strong disorder as a signature of AL below the mobility edge, slowing down the expansion.

This is supported by the experimental observation that the diffusion coefficient is of the order of only a few "quanta of diffusion" $\hbar/m$ [22,24,51]; see Fig. 3(d). Furthermore, with increasing $1/\tau_c \lesssim 1$ ms^{-1}, we see an initial plateau where neither diffusion exponent nor coefficient changes [shading in Figs. 3(c) and 3(d)]. It illustrates a strong suppression of the Fermi acceleration for sufficiently slow changes of the underlying disorder potential. The experimental observation is also in stark contrast to the classical simulation based on Fermi acceleration. We interpret this observation as the effect of localization due to wave function interference for small decorrelation rates.

To investigate the interplay of localization effects with superdiffusion or its suppression more closely, we estimate the fraction f_{loc} of localized atoms as introduced in Ref. [22]; see Appendix B in End Matter and Ref. [55]. We find a localized fraction of zero for the expansion in weak disorder even in the static case, as expected [inset of Fig. 3(b)]. By contrast, we find a significant $f_{loc} = (7.9 \pm 1.2)\%$ for the strong static disorder [inset of Fig. 3(d)]. This fraction decays as the decorrelation rate

$1/\tau_c$ increases, but as long as a localized fraction persists, the system shows close-to-normal diffusion. This restricted-diffusion plateau ends as soon as the localized fraction has decayed.

We interpret this plateau of α and D_α as a consequence of localization effects stabilizing diffusion against the disorder's accelerating dynamics. In fact, the energy scale $h/\tau_c \approx 48$ nK $\times k_B$ for the threshold $1/\tau_c \approx 1$ ms^{-1} is of the same order of magnitude as the energy associated with the critical momentum for AL, being $E_{AL} = \hbar^2 k_{AL}^2/2m \approx 115$ nK $\times k_B$ for the strong disorder and $\bar\eta$. This may explain why the observed plateau transitions to accelerated diffusion around $1/\tau_c \approx 1$ ms^{-1}. The fraction of particles with sufficiently low energy to localize despite the additional energy E_{AL} will be reduced with increasing $1/\tau_c$ until too few low-energy particles remain to influence the transport globally. Importantly, it remains unclear why Fermi acceleration can be efficiently suppressed even though more than 90% remain delocalized. This rather unexpected observation hints at deeper physics of dynamical phase transitions that has not yet been fully understood. Around $1/\tau_c \approx 1$ ms^{-1}, where f_{loc} has vanished, the acceleration becomes too strong to sustain coherent matter-wave interference and finally drives the system to superdiffusion. For the three largest values of $1/\tau_c$, we again observe $\alpha = 2$, consistent with the expected universal transport in time-dependent force fields, i.e., Fermi acceleration [36–38,44].

We have demonstrated a system that exhibits a broad tunability of anomalous diffusion during experimentally achievable timescales, ranging from subdiffusion to super-diffusion, reaching the regime of ballistic transport. Our findings elucidate intriguing quantum dynamics in time-varying random force fields, establishing an experimental platform to investigate Fermi acceleration in quantum systems. An interesting prospect will be to achieve $1/\tau_c$ timescales faster than the inverse Fermi energy. Then, we can explore the maximum-achievable rate of Fermi acceleration experimentally and discern whether our system tends asymptotically to the universal $\alpha = 2$ [38] or if hyper transport as in Ref. [31] is achievable. Further, a theoretical quantum many-body model of our system will be important to further understand the observed nonequilibrium transition from localization to acceleration, but is computationally costly; see End Matter for details. Such a computation is planned in future work on a high-performance cluster. Finally, since our system is capable of creating a strongly interacting Fermi gas along the crossover from a molecular Bose-Einstein condensate to a Bardeen-Cooper-Schrieffer superfluid [47,56], studying particle interactions and superfluidity will be a promising extension.

Data availability—The data that support the findings of this Letter are openly available [57].

[1] A. Einstein, *Investigations on the Theory of the Brownian Movement*, edited by R. Fürth (Dover Publications, New York, 1956).

[2] B. Duplantier, Brownian motion, "Diverse and Undulating", in *Einstein, 1905–2005: Poincaré Seminar 2005, Progress in Mathematical Physics*, edited by T. Damour, O. Darrigol, B. Duplantier, and V. Rivasseau (Birkhäuser, Basel, 2006), pp. 201–293.

[3] R. Metzler and J. Klafter, The random walk's guide to anomalous diffusion: A fractional dynamics approach, Phys. Rep. **339**, 1 (2000).

[4] G. Muñoz-Gil *et al.*, Objective comparison of methods to decode anomalous diffusion, Nat. Commun. **12**, 6253 (2021).

[5] V. Uchaikin and R. Sibatov, Fractional derivatives on cosmic scales, Chaos, Solitons Fractals **102**, 197 (2017).

[6] G. M. Viswanathan, V. Afanasyev, S. V. Buldyrev, E. J. Murphy, P. A. Prince, and H. E. Stanley, Lévy flight search patterns of wandering albatrosses, Nature (London) **381**, 413 (1996).

[7] A. M. Edwards, R. A. Phillips, N. W. Watkins, M. P. Freeman, E. J. Murphy, V. Afanasyev, S. V. Buldyrev, M. G. E. da Luz, E. P. Raposo, H. E. Stanley, and G. M. Viswanathan, Revisiting Lévy flight search patterns of wandering albatrosses, bumblebees and deer, Nature (London) **449**, 1044 (2007).

[8] V. Plerou, P. Gopikrishnan, L. A. Nunes Amaral, X. Gabaix, and H. E. Stanley, Economic fluctuations and anomalous diffusion, Phys. Rev. E **62**, R3023 (2000).

[9] R. Balescu, Anomalous transport in turbulent plasmas and continuous time random walks, Phys. Rev. E **51**, 4807 (1995).

[10] M. Di Pierro, D. A. Potoyan, P. G. Wolynes, and J. N. Onuchic, Anomalous diffusion, spatial coherence, and viscoelasticity from the energy landscape of human chromosomes, Proc. Natl. Acad. Sci. U.S.A. **115**, 7753 (2018).

[11] P. W. Anderson, Absence of diffusion in certain random lattices, Phys. Rev. **109**, 1492 (1958).

[12] *50 Years of Anderson Localization*, edited by E. Abrahams (World Scientific, Singapore, 2010).

[13] R. Weaver, Anderson localization of ultrasound, Wave Motion **12**, 129 (1990).

[14] H. Hu, A. Strybulevych, J. H. Page, S. E. Skipetrov, and B. A. van Tiggelen, Localization of ultrasound in a three-dimensional elastic network, Nat. Phys. **4**, 945 (2008).

[15] R. Dalichaouch, J. P. Armstrong, S. Schultz, P. M. Platzman, and S. L. McCall, Microwave localization by two-dimensional random scattering, Nature (London) **354**, 53 (1991).

[16] D. S. Wiersma, P. Bartolini, A. Lagendijk, and R. Righini, Localization of light in a disordered medium, Nature (London) **390**, 671 (1997).

[17] F. Scheffold, R. Lenke, R. Tweer, and G. Maret, Localization or classical diffusion of light?, Nature (London) **398**, 206 (1999).

[18] T. Schwartz, G. Bartal, S. Fishman, and M. Segev, Transport and Anderson localization in disordered two-dimensional photonic lattices, Nature (London) **446**, 52 (2007).

[19] A. Mafi and J. Ballato, Review of a decade of research on disordered anderson localizing optical fibers, Front. Phys. **9** (2021).

[20] J. Billy, V. Josse, Z. Zuo, A. Bernard, B. Hambrecht, P. Lugan, D. Clément, L. Sanchez-Palencia, P. Bouyer, and A. Aspect, Direct observation of Anderson localization of matter waves in a controlled disorder, Nature (London) **453**, 891 (2008).

[21] G. Roati, C. D'Errico, L. Fallani, M. Fattori, C. Fort, M. Zaccanti, G. Modugno, M. Modugno, and M. Inguscio, Anderson localization of a non-interacting Bose–Einstein condensate, Nature (London) **453**, 895 (2008).

[22] F. Jendrzejewski, A. Bernard, K. Müller, P. Cheinet, V. Josse, M. Piraud, L. Pezzé, L. Sanchez-Palencia, A. Aspect, and P. Bouyer, Three-dimensional localization of ultracold atoms in an optical disordered potential, Nat. Phys. **8**, 398 (2012).

[23] S. S. Kondov, W. R. McGehee, J. J. Zirbel, and B. DeMarco, Three-dimensional Anderson localization of ultracold matter, Science **334**, 66 (2011).

[24] B. Shapiro, Cold atoms in the presence of disorder, J. Phys. A **45**, 143001 (2012).

[25] C. A. Müller and B. Shapiro, Comment on "three-dimensional anderson localization in variable scale disorder", Phys. Rev. Lett. **113**, 099601 (2014).

[26] J. Šuntajs, J. Bonča, T. c. v. Prosen, and L. Vidmar, Quantum chaos challenges many-body localization, Phys. Rev. E **102**, 062144 (2020).

[27] M. Kiefer-Emmanouilidis, R. Unanyan, M. Fleischhauer, and J. Sirker, Evidence for unbounded growth of the number entropy in many-body localized phases, Phys. Rev. Lett. **124**, 243601 (2020).

[28] J. Léonard, S. Kim, M. Rispoli, A. Lukin, R. Schittko, J. Kwan, E. Demler, D. Sels, and M. Greiner, Probing the onset of quantum avalanches in a many-body localized system, Nat. Phys. **19**, 481 (2023).

[29] D. A. Evensky, R. T. Scalettar, and P. G. Wolynes, Localization and dephasing effects in a time-dependent Anderson Hamiltonian, J. Phys. Chem. **94**, 1149 (1990).

[30] S. Lorenzo, T. Apollaro, G. M. Palma, R. Nandkishore, A. Silva, and J. Marino, Remnants of Anderson localization in

prethermalization induced by white noise, Phys. Rev. B **98**, 054302 (2018).

[31] L. Levi, Y. Krivolapov, S. Fishman, and M. Segev, Hyper-transport of light and stochastic acceleration by evolving disorder, Nat. Phys. **8**, 912 (2012).

[32] E. Fermi, On the origin of the cosmic radiation, Phys. Rev. **75**, 1169 (1949).

[33] P. A. Sturrock, Model of the high-energy phase of solar flares, Nature (London) **211**, 695 (1966).

[34] M. Ostrowski and G. Siemieniec-Oziębło, Diffusion in momentum space as a picture of second-order Fermi acceleration, Astropart. Phys. **6**, 271 (1997).

[35] P. Mertsch and S. Sarkar, Fermi gamma-ray "bubbles" from stochastic acceleration of electrons, Phys. Rev. Lett. **107**, 091101 (2011).

[36] L. Golubović, S. Feng, and F.-A. Zeng, Classical and quantum superdiffusion in a time-dependent random potential, Phys. Rev. Lett. **67**, 2115 (1991).

[37] M. N. Rosenbluth, Comment on "Classical and quantum superdiffusion in a time-dependent random potential", Phys. Rev. Lett. **69**, 1831 (1992).

[38] B. Aguer, S. De Bièvre, P. Lafitte, and P. E. Parris, Classical motion in force fields with short range correlations, J. Stat. Phys. **138**, 780 (2010).

[39] G. Volpe, G. Volpe, and S. Gigan, Brownian motion in a speckle light field: Tunable anomalous diffusion and selective optical manipulation, Sci. Rep. **4**, 3936 (2014).

[40] S. M. Ulam, On some statistical properties of dynamical systems, in *Contributions to Astronomy, Meteorology, and Physics*, edited by J. Neyman (University of California Press, Berkeley, California, 1961), pp. 315–320.

[41] A. J. Lichtenberg and M. A. Lieberman, *Regular and Stochastic Motion*, edited by F. John, J. E. Marsden, and L. Sirovich, Applied Mathematical Sciences, Vol. 38 (Springer, New York, 1983).

[42] J. V. José and R. Cordery, Study of a quantum fermi-acceleration model, Phys. Rev. Lett. **56**, 290 (1986).

[43] P. Seba, Quantum chaos in the Fermi-accelerator model, Phys. Rev. A **41**, 2306 (1990).

[44] F. Bouchet, F. Cecconi, and A. Vulpiani, Minimal stochastic model for Fermi's acceleration, Phys. Rev. Lett. **92**, 040601 (2004).

[45] L. Beilin, E. Gurevich, and B. Shapiro, Diffusion of cold-atomic gases in the presence of an optical speckle potential, Phys. Rev. A **81**, 033612 (2010).

[46] K. Abbas and A. Boudjemâa, Binary Bose–Einstein condensates in a disordered time-dependent potential, J. Phys. Condens. Matter **34**, 125102 (2022).

[47] B. Gänger, J. Phieler, B. Nagler, and A. Widera, A versatile apparatus for fermionic lithium quantum gases based on an interference-filter laser system, Rev. Sci. Instrum. **89**, 093105 (2018).

[48] B. Nagler, M. Will, S. Hiebel, S. Barbosa, J. Koch, M. Fleischhauer, and A. Widera, Ultracold Bose gases in dynamic disorder with tunable correlation time, Phys. Rev. Lett. **128**, 233601 (2022).

[49] S. Hiebel, B. Nagler, S. Barbosa, J. Koch, and A. Widera, Characterizing quantum gases in time-controlled disorder realizations using cross-correlations of density distributions, New J. Phys. **26**, 013042 (2024).

[50] B. Nagler, S. Barbosa, J. Koch, G. Orso, and A. Widera, Observing the loss and revival of long-range phase coherence through disorder quenches, Proc. Natl. Acad. Sci. U.S.A. **119** (2022).

[51] R. C. Kuhn, O. Sigwarth, C. Miniatura, D. Delande, and C. A. Müller, Coherent matter wave transport in speckle potentials, New J. Phys. **9**, 161 (2007).

[52] See Supplemental Material at http://link.aps.org/supplemental/10.1103/rq4w-377l for technical details on the experiment, a description of the cloud-width extraction, and an extended simulation evaluation.

[53] S. Pilati, S. Giorgini, M. Modugno, and N. Prokof'ev, Dilute Bose gas with correlated disorder: A path integral Monte Carlo study, New J. Phys. **12**, 073003 (2010).

[54] L. Sanchez-Palencia, D. Clément, P. Lugan, P. Bouyer, and A. Aspect, Disorder-induced trapping versus Anderson localization in Bose–Einstein condensates expanding in disordered potentials, New J. Phys. **10**, 045019 (2008).

[55] S. Barbosa, M. Kiefer-Emmanouilidis, F. Lang, J. Koch, and A. Widera, Characterizing localization effects in an ultra-cold disordered Fermi gas by diffusion analysis, Phys. Rev. Res. **6**, 033039 (2024).

[56] J. Koch, K. Menon, E. Cuestas, S. Barbosa, E. Lutz, T. Fogarty, T. Busch, and A. Widera, A quantum engine in the BEC–BCS crossover, Nature (London) **621**, 723 (2023).

[57] S. Barbosa, M. Kiefer-Emmanouilidis, F. Lang, J. Koch, and A. Widera, Zenodo repository: https://zenodo.org/doi/10.5281/zenodo.10478890.

End Matter

Appendix A: Markov-Chain Monte Carlo simulation— As stated in the main text, the simulations are based on the model presented in Ref. [44]. We simulate classical nonrelativistic point particles colliding elastically with hard-sphere scatterers of infinite mass on a flat two-dimensional plane. The initial particle velocities are distributed according to the Fermi-Dirac distribution, approximating the experimental setting as closely as possible, while the movement of the spheres mimics the dynamics of our time-dependent speckle. We choose a 2D system since, in 1D, the mechanism of Fermi acceleration is significantly different due to the lack of scattering angles. Single scattering events are effectively the same for dimensions larger than one if the scattering angles are assumed uniformly distributed. Since our atom cloud is three-dimensional, we simulate in $d > 1$ and choose $d = 2$ as a compromise to save computing resources.

In the case of frozen scattering centers, normal diffusion is the result. However, when these scatterers themselves are moving, the particles undergo Fermi acceleration and expand superdiffusively. Since here and in contrast to the experimental setup, we do have access to the trajectories $\mathbf{r}(t)$ of each particle, we directly calculate the mean-squared displacement (MSD) as

$$\text{MSD}(t) = \langle \mathbf{r}^2 \rangle(t) - \langle \mathbf{r}^2 \rangle(0), \tag{A1}$$

where $\langle \cdot \rangle$ denotes the average over the particles. For each simulation run, we set 1000 particles, each colliding 25000 times with the randomly moving spheres. Finally, we run such a series 12 times and average the diffusion exponents and coefficients extracted from each series.

We choose values as close to the experimental setting as possible for the scatterers. As their radius, we use the geometric mean of our disorder's correlation lengths $\bar{\eta}$ and use the average distance of speckle peaks, $3\bar{\eta}$, for their density $\rho = 1/(3\bar{\eta})^2$. Since the speckle's spatial intensity is exponentially distributed, we assumed that the same holds for the velocity. Therefore, the simulated scatterers' velocity is determined randomly with an exponential probability

distribution. Note that the choice of their velocity distribution has little to no impact on the result. Only the average velocity has a significant influence. Therefore, we iterate through 25 different values of their average velocity between zero [see black line A in Fig. 2(c)] and the maximum value (yellow line B) of $v_{\text{sim}}^{\max} = 6.3 \text{ mm s}^{-1}$. That value is estimated from the velocity scale of our maximally dynamic disorder by comparing the present length and timescales $\bar{\eta}/\tau_c$ for $1/\tau_c = 3.5 \text{ ms}^{-1}$. For the initial spatial distribution of the point particles, we choose a Gaussian with $\sigma_{x,y}(0) = 50$ mµ. For their velocity magnitudes, we distribute values between zero and the Fermi velocity v_F of our experimental system as they would be for an ideal Fermi gas, while the angles are chosen isotropically. Note that, except for the cases of static (where only the direction but not the magnitude of the velocity vector can change) or absent scatterers, its choice has a negligible influence on the expansion due to the underlying Markov assumption.

Even though we insert the various scales of our experiment as closely as possible, we emphasize that the simulation still describes a very different setting from our system. Still, employing the simulation reinforces the assumption that Fermi acceleration is the underlying mechanism driving our atoms to superdiffusion.

Finally, we note that a many-body theory taking into account the full quantum nature of the Fermi gas will be important for an in-depth evaluation of the observed transition from a localized to an accelerated gas. Such a model must incorporate small-scale yet strong disorder that varies smoothly and continuously over short timescales. Additionally, it must account for the initial many-body ground-state wave function and the energy distribution within the disordered Fermi sea of 10^5 particles.

Appendix B: Localized fraction— The localized fraction f_{loc} estimates the infinite-time fraction of atoms that would not diffuse away due to being localized, assuming no atom losses. We base the determination of
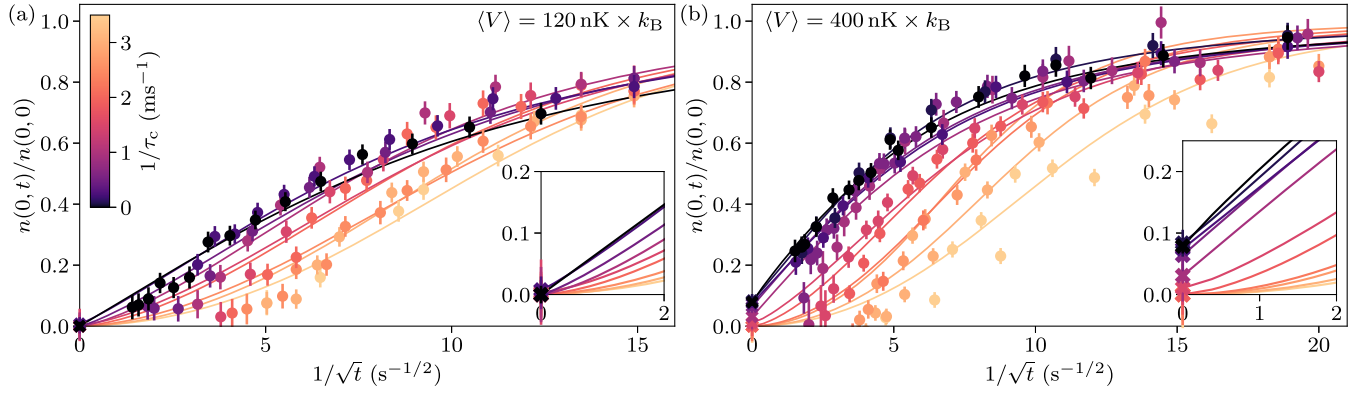
FIG. 4. Determining the localized fraction f_{loc} from the series with (a) weak disorder, $\langle V \rangle = 120$ nK $\times k_{\text{B}}$, and (b) strong disorder, $\langle V \rangle = 400$ nK $\times k_{\text{B}}$. Plotting the relative density $n(t)/n(0)$ (circles) over the square root of inverse time allows us to visualize f_{loc} as the density-axis intercept (crosses at $1/\sqrt{t} = 0$). Lines are fits with the anomalous-diffusion model Eq. (B1) where f_{loc}, the value of the density for $t \rightarrow \infty$, is the only free parameter. Errors are calculated from error propagation. The insets show the same as enlargements of the density-axis intercepts of the fit lines for enhanced visibility of how f_{loc} emerges from the fits.

the localized fraction on the method reported in Ref. [22], modified for our expansion along one dimension. Assuming a purely diffusive setting and a unimodal atom distribution, the cloud's peak density $n(y = 0, t)$ decreases in time with $1/\sigma(t)$. Specifically, we compute the relative peak density $n(0,t)/n(0,t=0) = \sigma(0)/\sigma(t)$, such that all remaining factors cancel out irrespective of the specific underlying distribution. We further adjusted the method of Ref. [22] by implementing the full anomalous-diffusion power law for $\sigma(t)$ as in Eq. (1). Then, any remaining fraction of the relative peak density in the limit of $t \rightarrow \infty$ is interpreted as the localized fraction f_{loc}, i.e., the deviation from the purely diffusive picture. Specifically, we use the model

$$\frac{n(0,t)}{n(0,0)} = f_{\text{loc}} + (1 - f_{\text{loc}}) \sqrt{\frac{\sigma^2(0)}{2D_\alpha t^\alpha + \sigma^2(0)}}, \quad \text{(B1)}$$

where we fix the diffusion exponent α and coefficient D_α to the values we extract as described in the text and use $\sigma(0) = 53$ μm from a Gauss fit to the trapped cloud. For the relative peak density $n(0,t)/n(0,0)$, we use the approximation of $n(0,t) \approx w(t) - w_{\text{noise}}$ with an additional factor of $N(0)/N(t)$ to compensate for atom losses, where $w(t)$ and w_{noise} are the so-called histogram widths of the density profile at time t and pure-noise profile, respectively. We find this approximation to be quite robust against image noise. Note that we describe the histogram quantities as well as the inverse participation width in more detail in Supplemental Material [52]. Further, for a comprehensive introduction and discussion of these quantities including a systematic comparison with established observables, see our previous work in Ref. [55]. Finally, we emphasize that we extract f_{loc} as the only free parameter from fitting the right side of Eq. (B1); see Fig. 4.